

## X-ray Coronal Properties of Swift/BAT-Selected Seyfert 1 Active Galactic Nuclei

NIKITA KAMRAJ,<sup>1</sup> MURRAY BRIGHTMAN,<sup>1</sup> FIONA A. HARRISON,<sup>1</sup> DANIEL STERN,<sup>2</sup> JAVIER A. GARCÍA,<sup>1,3</sup>  
MISLAV BALOKOVIĆ,<sup>4,5</sup> CLAUDIO RICCI,<sup>6,7,8</sup> MICHAEL J. KOSS,<sup>9,10</sup> JULIAN E. MEJÍA-RESTREPO,<sup>11</sup> KYUSEOK OH,<sup>12,13,14</sup>  
MEREDITH C. POWELL,<sup>15</sup> AND C. MEGAN URRY<sup>4,5</sup>

<sup>1</sup>*Cahill Center for Astronomy and Astrophysics, California Institute of Technology, Pasadena, CA 91125, USA*

<sup>2</sup>*Jet Propulsion Laboratory, California Institute of Technology, Pasadena, CA 91109, USA*

<sup>3</sup>*Dr. Karl Remeis-Observatory and Erlangen Centre for Astroparticle Physics, Sternwartstr 7, D-96049 Bamberg, Germany*

<sup>4</sup>*Yale Center for Astronomy & Astrophysics, 52 Hillhouse Avenue, New Haven, CT 06511, USA*

<sup>5</sup>*Department of Physics, Yale University, PO Box 208120, New Haven, CT 06520, USA*

<sup>6</sup>*Núcleo de Astronomía de la Facultad de Ingeniería, Universidad Diego Portales, Av. Ejército Libertador 441, Santiago 22, Chile*

<sup>7</sup>*Kavli Institute for Astronomy and Astrophysics, Peking University, Beijing 100871, People's Republic of China*

<sup>8</sup>*George Mason University, Department of Physics & Astronomy, MS 3F3, 4400 University Drive, Fairfax, VA 22030, USA*

<sup>9</sup>*Eureka Scientific, 2452 Delmer Street Suite 100, Oakland, CA 94602-3017, USA*

<sup>10</sup>*Space Science Institute, 4750 Walnut Street, Suite 205, Boulder, Colorado 80301, USA*

<sup>11</sup>*European Southern Observatory, Casilla 19001, Santiago 19, Chile*

<sup>12</sup>*Korea Astronomy & Space Science institute, 776, Daedeokdae-ro, Yuseong-gu, Daejeon 34055, Republic of Korea*

<sup>13</sup>*Department of Astronomy, Kyoto University, Kitashirakawa-Oiwake-cho, Sakyo-ku, Kyoto 606-8502, Japan*

<sup>14</sup>*JSPS Fellow*

<sup>15</sup>*Kavli Institute of Particle Astrophysics and Cosmology, Stanford University, 452 Lomita Mall, Stanford, CA 94305, USA*

### ABSTRACT

The corona is an integral component of Active Galactic Nuclei (AGN) which produces the bulk of the X-ray emission above 1–2 keV. However, many of its physical properties and the mechanisms powering this emission remain a mystery. In particular, the temperature of the coronal plasma has been difficult to constrain for large samples of AGN, as constraints require high quality broadband X-ray spectral coverage extending above 10 keV in order to measure the high energy cutoff, which provides constraints on the combination of coronal optical depth and temperature. We present constraints on the coronal temperature for a large sample of Seyfert 1 AGN selected from the *Swift*/BAT survey using high quality hard X-ray data from the *NuSTAR* observatory combined with simultaneous soft X-ray data from *Swift*/XRT or *XMM-Newton*. When applying a physically-motivated, non-relativistic disk reflection model to the X-ray spectra, we find a mean coronal temperature  $kT_e = 84 \pm 9$  keV. We find no significant correlation between the coronal cutoff energy and accretion parameters such as the Eddington ratio and black hole mass. We also do not find a statistically significant correlation between the X-ray photon index,  $\Gamma$ , and Eddington ratio. This calls into question the use of such relations to infer properties of supermassive black hole systems.

*Keywords:* galaxies: active – galaxies: Seyfert – X-rays: galaxies

### 1. INTRODUCTION

Active Galactic Nuclei (AGN) are known to produce copious amounts of hard X-ray radiation. This continuum X-ray emission is believed to be produced in a hot cloud of plasma called the *corona*, where electrons

Compton up-scatter thermal optical and UV photons from the accretion disk to X-ray energies (e.g., Haardt & Maraschi 1993; Merloni & Fabian 2001). While many of its physical properties are not well constrained, the corona is known to be compact, of the order of 3–10  $R_g$  (where  $R_g = GM_{\text{BH}}/c^2$  is the gravitational radius for a black hole of mass  $M_{\text{BH}}$ ), as determined by methods such as rapid X-ray variability (e.g., McHardy et al. 2005), quasar microlensing (e.g., Chartas et al. 2016),

and reverberation mapping of X-ray radiation reprocessed by the accretion disk (e.g., Fabian et al. 2009; De Marco et al. 2013; Uttley et al. 2014). AGN coronae may also be compact in a radiative sense, indicating an abundance of interactions involving significant energy exchange between particles and photons within the source (Fabian et al. 2015). This radiative compactness can be characterized by the dimensionless parameter  $l$  (Guilbert et al. 1983), defined as:

$$l = 4\pi \frac{m_p}{m_e} \frac{R_g}{R} \frac{L}{L_E} \quad (1)$$

where  $m_p$  and  $m_e$  are the proton and electron mass respectively,  $R_g$  is the gravitational radius,  $R$  is the coronal radius,  $L$  is the coronal luminosity, and  $L_E$  is the Eddington luminosity.

Some of the fundamental physical properties of the corona, such as its temperature ( $kT_e$ ) and optical depth ( $\tau$ ) can be probed through broadband X-ray spectroscopy. Specifically, the coronal X-ray emission can be characterized by a high-energy cutoff,  $E_{\text{cut}}$ , when approximating the X-ray continuum flux as a power law  $\propto E^{-\Gamma} e^{-E/E_{\text{cut}}}$ , where  $E$  is the photon energy and  $\Gamma$  is the continuum photon index (e.g., Rothschild et al. 1983). Spectral parameters obtained from broadband X-ray fitting thus correspond to physical parameters of the corona, with the temperature related to the cutoff energy via  $E_{\text{cut}} \sim 2-3 kT_e$ , assuming a slab-like coronal geometry (Petrucci et al. 2001). Measurements of the cutoff energy have been difficult to obtain, since they require high-quality broadband X-ray spectral coverage above 10 keV. Previous studies of  $E_{\text{cut}}$  performed with non-focusing/collimating X-ray instruments in the hard X-ray band such as *CGRO/OSSE* (e.g., Rothschild et al. 1983; Zdziarski et al. 2000), *BeppoSAX* (e.g., Nicastro et al. 2000; Dadina 2007) and *INTEGRAL* (e.g., Beckmann et al. 2009; Ricci et al. 2011; Malizia et al. 2014; Lubiński et al. 2016) had limited sensitivity and could only constrain  $E_{\text{cut}}$  for the brightest nearby AGN.

The launch of the *NuSTAR* observatory (Harrison et al. 2013) has transformed measurements of AGN cutoff energies. Being the first focusing hard X-ray telescope in orbit with spectral coverage up to 79 keV, *NuSTAR* has enabled  $E_{\text{cut}}$  to be constrained for many individual unobscured and obscured AGN (e.g., Ballantyne et al. 2014; Brenneman et al. 2014; Baloković et al. 2015; Kara et al. 2017; Xu et al. 2017). The *Swift*/BAT catalog (e.g., Gehrels et al. 2004; Baumgartner et al. 2013; Oh et al. 2018) provides a large sample of local, bright AGN with uniform sky coverage. Several studies have presented X-ray spectral analyses of *Swift*/BAT-selected AGN to investigate physical properties of the accreting

supermassive black hole (SMBH). For example, Ricci et al. (2017) performed a broadband spectral analysis of 836 *Swift*/BAT AGN and found a median cutoff energy for the entire sample of  $E_{\text{cut}} = 200 \pm 29$  keV; however, these measurements did not use *NuSTAR* data and primarily utilised lower quality hard X-ray data from non-focusing instruments such as *Swift*/BAT. Kamraj et al. (2018) presented  $E_{\text{cut}}$  constraints for a sample of 46 *Swift*/BAT-selected Seyfert 1 AGN using  $\sim 20$  ks exposure *NuSTAR* snapshot observations performed as part of the *NuSTAR* Extragalactic Legacy Surveys program<sup>1</sup>. More recently, Baloković et al. (2020) presented  $E_{\text{cut}}$  constraints for obscured AGN selected from the *Swift*/BAT catalog, that also have short, 20 ks *NuSTAR* exposures.

In addition to constraining cutoff energies, *NuSTAR* has revitalized deeper exploration of AGN coronal parameters and their possible connection with the accretion properties of SMBH systems, such as the associated Eddington ratio. While some past studies of AGN that did not utilize *NuSTAR* measurements have found tentative correlations between median values of  $E_{\text{cut}}$  and accretion parameters such as the Eddington ratio (e.g., Ricci et al. 2018), studies of small samples of AGN observed with *NuSTAR* have shown no evidence for such a correlation (Tortosa et al. 2018).

In this paper, we present the first systematic study of the coronal properties of a large sample of unobscured AGN observed with *NuSTAR*. We use 195 observations of Seyfert 1 AGN selected from the *Swift*/BAT all-sky survey that also have snapshot *NuSTAR* legacy observations or long exposure targets observed as part of individual Guest Observer programs. We include simultaneous soft X-ray data from the *Swift*/XRT and *XMM-Newton* instruments where available. This study provides a combination of superior quality broadband X-ray data with a large sample size, enabling robust characterization of the physical properties of the corona in the local, unobscured AGN population.

This paper is structured as follows: in section 2 we describe the sample used in this work, the X-ray observations, and data reduction procedures; in section 3 we detail the various spectral models considered for fitting to the broadband X-ray data; in section 4 we present constraints on coronal temperatures for our sample and investigate the relation between parameters derived from spectral fitting and accretion properties such as Eddington ratio and black hole mass; we summarize our find-

<sup>1</sup> [https://www.nustar.caltech.edu/page/legacy\\_surveys](https://www.nustar.caltech.edu/page/legacy_surveys)

ings in section 5. We quote parameter uncertainties from spectral fitting at the 90% confidence level.

## 2. SAMPLE, OBSERVATIONS AND DATA REDUCTION

### 2.1. Seyfert 1 Sample

For this study, we selected sources by choosing AGN from the *Swift*/BAT 70-month X-ray catalog (Baumgartner et al. 2013). The all-sky catalog consists of AGN that are bright in the hard X-ray band (14–195 keV). Among these sources, we select AGN that are optically classified as Seyfert 1 (Sy1), a sample that contains sub-classes ranging from Sy1–Sy1.8, following the Osterbrock classification system (Osterbrock 1981). The optical spectroscopic classification is derived from the BAT AGN Spectroscopic Survey (BASS;<sup>2</sup> Koss et al. (2017)). From this sample of unobscured AGN we then selected sources that had been observed by *NuSTAR*, both as part of the Extragalactic Legacy Survey and Guest Observer program observations. Our final sample contains 195 Sy 1 AGN with redshifts in the range  $0.002 < z < 0.2$ . In addition to the *NuSTAR* observations, where available we utilize simultaneous soft X-ray data in the 0.4–10 keV band taken with either the *Swift*/XRT or *XMM-Newton*/EPIC instruments.

### 2.2. *NuSTAR*

We performed reduction of the raw event data from both *NuSTAR* modules, FPMA and FPMB (Harrison et al. 2013) using the *NuSTAR* Data Analysis Software (*NuSTAR*DAS, version 2.14.1), distributed by the NASA High-Energy Astrophysics Archive Research Center (HEASARC) within the HEASOFT package, version 6.27. We calculated instrumental responses based on the *NuSTAR* calibration database (CALDB), version 20180925. We cleaned and filtered raw event data for South Atlantic Anomaly (SAA) passages using the *nupipeline* module. We then extracted source and background spectra from the calibrated and cleaned event files using the *nuproducts* module. More detailed information on these data reduction procedures can be found in the *NuSTAR* Data Analysis Software Guide (Perri et al. 2017). Source spectra were extracted from circular regions with an extraction radius ranging from 30'' to 60'' depending on the source size and brightness. We extracted background spectra from source-free regions of the image on the same detector chip as the source, away from the outer edges of the field of view, which have systematically higher background.

<sup>2</sup> <https://www.bass-survey.com/>

### 2.3. *XMM-Newton*

In addition to the *NuSTAR* hard X-ray data, where available we utilize simultaneous observations from the *XMM-Newton* observatory (Jansen et al. 2001) in the soft X-ray band taken with the EPIC-pn detector (Strüder et al. 2001). We have simultaneous *XMM-Newton* observations for 26 observations in our sample. We performed reduction of the raw *XMM-Newton* data using the *XMM-Newton* Science Analysis System (SAS, Gabriel et al. 2004, version 16.1.0), following the standard prescription outlined in the *XMM-Newton* ABC online guide.<sup>3</sup> Calibrated, cleaned event files were created from the raw data files using the SAS command *epchain* for the EPIC-pn detector. As recommended, we only extracted single and double pixel events for EPIC-pn. Source spectra were extracted from the cleaned event files using the SAS task *xmmselect*. Background spectra were extracted from a circular aperture placed near the source on the same CCD chip. We checked for the presence of detector pileup using the SAS task *EPATPLOT*. Where significant pileup was detected in an observation we used an annular extraction region in which the core of the source point spread function is excised in order to remove pileup. We generated instrumental response files using the SAS tasks *rmfgen* and *arfgen*.

### 2.4. *Swift*/XRT

For sources where simultaneous soft X-ray coverage with *XMM-Newton* was not available, we use simultaneous data taken with the *Swift*/XRT instrument (Burrows et al. 2005). We have simultaneous *Swift*/XRT observations for 149 observations in our sample. We reduced the *Swift*/XRT data using the ASDC XRT Online Analysis service<sup>4</sup>. We performed standard filtering using the *XRTPIPELINE* script following the guidelines detailed in Evans et al. (2009). We extracted background spectra from large annular regions around the source, taking care to avoid contamination. Instrumental ARF and RMF response files were generated using the *XRTPRODUCTS* script.

## 3. X-RAY SPECTRAL MODELING

We performed all spectral modeling of the broadband X-ray data using the XSPEC fitting tool (v12.11, Arnaud 1996). We adopt cross sections from Verner et al. (1996) and solar abundances from Wilms et al. (2000). In all our model fitting we include a Galac-

<sup>3</sup> <https://heasarc.gsfc.nasa.gov/docs/xmm/abc/>

<sup>4</sup> <http://www.asdc.asi.it/mmia/index.php?mission=swiftmastr>

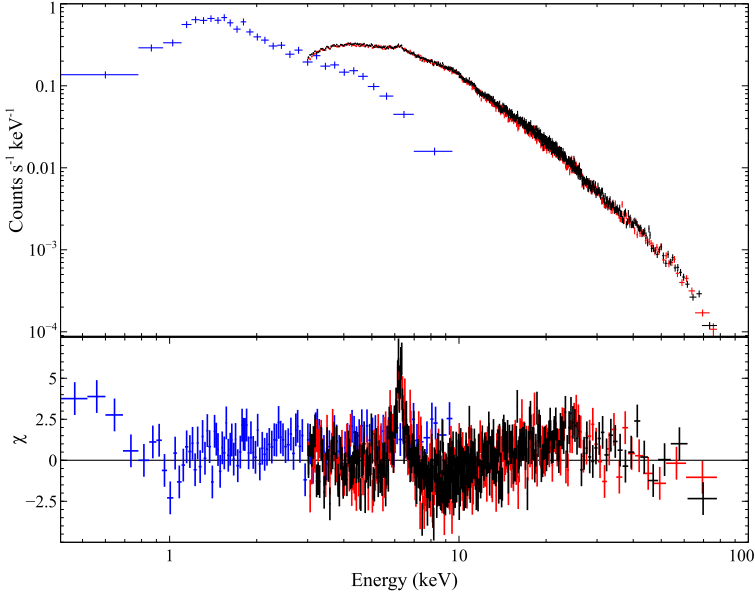


**Figure 1.** Broadband X-ray spectrum of IC4329A (top) alongside fit residuals for an absorbed cutoff power law model (bottom). Blue points represents *Swift*/XRT data while black and red points correspond to *NuSTAR* FPMA and FPMB data respectively. Data points are re-binned for plotting clarity.

tic absorption component modeled with the TBABS absorption code (Wilms et al. 2000), using Galactic column densities  $N_{\text{H, Gal}}$  taken from the HI maps of the LAB survey (Kalberla et al. 2005). We also add a cross-normalization constant factor ( $c_{\text{ins}}$ ) to all models to account for variability and calibration uncertainties across different instruments.

### 3.1. Model 1: Simple Absorbed Power Law

The first model we employ consists of a simple absorbed power law continuum with a high-energy cutoff  $E_{\text{cut}}$ . The power law continuum slope is characterized by the photon index  $\Gamma$ , with the intrinsic continuum flux proportional to  $E^{-\Gamma} \exp(-E/E_{\text{cut}})$ . In XSPEC notation, the model is given by  $c_{\text{ins}} \times \text{TBABS} \times \text{ZPHABS} \times \text{CUTOFFPL}$ , where ZPHABS models photoelectric host galaxy absorption. Figure 1 presents an example broadband X-ray spectrum for one of the sources in our sample, alongside residuals to the absorbed power law model fit to the data.

### 3.2. Model 2: Phenomenological Reflection (PEXRAV)

The second model we apply accounts for reflection features in the X-ray spectrum from reprocessing of the hard X-ray emission, such as the Fe  $K\alpha$  line at a rest-frame energy of 6.4 keV and Compton reflection hump peaking around 20–30 keV (see e.g. Figure 1).

We model these features using the phenomenological PEXRAV model (Magdziarz & Zdziarski 1995), which assumes reflection off a slab of semi-infinite extent and optical depth. Our model expression in XSPEC is given by  $c_{\text{ins}} \times \text{TBABS} \times \text{ZPHABS} \times (\text{CUTOFFPL} + \text{ZGAUSS} + \text{PEXRAV})$ , where ZGAUSS models a Gaussian Fe  $K\alpha$  line. We fix iron and light element abundances to solar values and fix the inclination angle of the plane of reflecting material at the default value of  $\cos \theta = 0.45$ . We tie the photon index and normalization of the reflected power law to that of the incident power law and fix the energy of the Fe  $K\alpha$  line at 6.4 keV.

### 3.3. Model 3: Physical Reflection (XILLVERCP) Model

The final model we apply is an advanced reflection model that accurately models the physics of reprocessed radiation from the corona. We replace the PEXRAV component with the XILLVERCP model (García & Kallman 2010), which forms part of the RELXILL family of disk reflection models (García et al. 2014). These models adopt a rich atomic database, fully calculate the angular distribution of the reflected radiation and provide various geometrical models of the illuminating coronal source. The XILLVERCP model treats the coronal radiation incident on the disk as a thermally Comptonized continuum using the NTHCOMP code (Zdziarski et al. 1996) which vastly improves over a simple exponential cutoff power law continuum approximation. The model also self-consistently calculates the relative strength of the reflected emission,  $R$ , and the ionization parameter of the accretion disk, defined as  $\xi = 4\pi F_X/n$  where  $F_X$  is the incident X-ray flux and  $n$  is the disk density. A disk density of  $10^{15} \text{ cm}^{-3}$  is assumed for the XILLVERCP model. Other key free parameters are the photon index  $\Gamma$  and the coronal electron temperature  $kT_e$ . We fix the inclination angle measured with respect to the disk normal at the default value of  $30^\circ$ . These advanced reflection models are able to provide constraints on the coronal temperature up to several hundred keV, past the limit of the *NuSTAR* detector bandpass, since the ionization state and disk structure are conditioned by the high-energy region of the spectrum, which in turn determines the observed reflection features.

### 3.4. Choice of Spectral Fitting Statistic

In our model fitting, we consider both  $\chi^2$  statistics and the Cash statistic (C-stat, Cash 1979). While  $\chi^2$  statistics have traditionally been used as the primary fit statistic for X-ray spectral fitting, its usage is appropriate only when there are sufficient photon counts in a given energy bin such that the statistical variations can be approximated by a Gaussian distribution. Rebinning of spectra to achieve a Gaussian approximation can

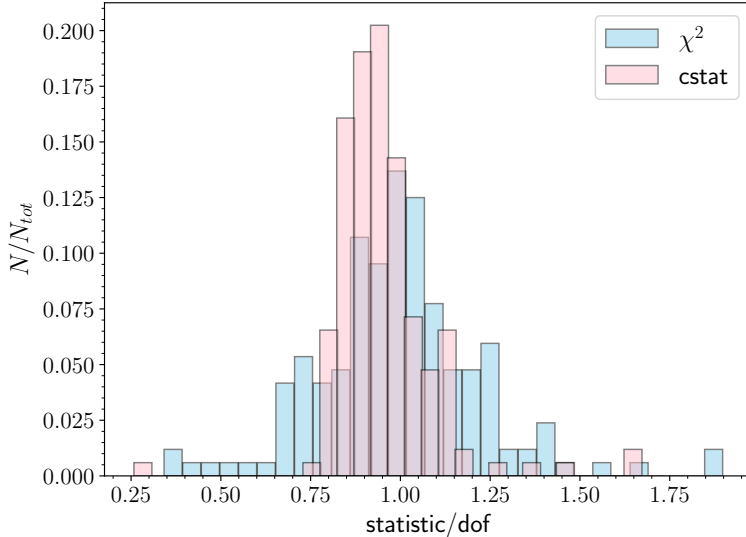


**Figure 2.** Distributions of the goodness-of-fit for the  $\chi^2$  and Cash statistics (C-stat) for an absorbed power law model fit (Model 1) to the broadband X-ray data for our entire sample.

thus wash out key features in the X-ray spectrum, such as curvature at high energies from which estimations of  $E_{\text{cut}}$  are made. A more appropriate fit statistic to use, particularly when dealing with low photon counts, is C-stat, which maintains Poisson counting statistics and provides unbiased parameter estimation while still resembling a  $\chi^2$  statistic (Kaastra 2017).

When applying  $\chi^2$  statistics, we rebinned the *NuSTAR* data to give a minimum of 20 photon counts per bin. For C-stat, we rebinned the data to have unity photon count per bin. We used the HEASOFT task `grppha` for all spectral binning. In Figure 2 we show the distribution of the goodness of fit (defined as the value of the fit statistic divided by the number of degrees of freedom) for both  $\chi^2$  and C-statistics, when applying the absorbed power law model fit to the data for our sample. We find that the distribution of the goodness of fit has a similar mean value for both types of statistic, indicating that C-stat provides an equally valid goodness of fit measure compared to  $\chi^2$  statistics. In addition, the goodness of fit is more tightly distributed around unity for C-stat, thus providing an overall better fit, motivating its usage as the primary fit statistic for our work.

## 4. RESULTS AND DISCUSSION

### 4.1. Distribution of High Energy Cutoffs

We examined the distributions of coronal cutoff energies determined from broadband X-ray modeling ( $E_{\text{cut}}$  or  $kT_e$  depending on type of spectral model) for our full sample, considering both best-fit values and lower

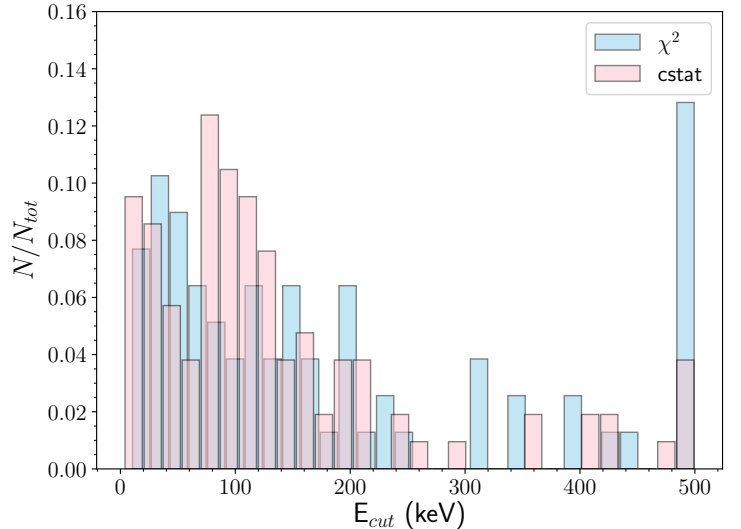


**Figure 3.** Distributions of the high energy cutoff  $E_{\text{cut}}$  for the  $\chi^2$  and Cash statistics (C-stat) for an absorbed power law model fit (Model 1) to the broadband X-ray data for our entire sample. We note that the model limit for the value of  $E_{\text{cut}}$  is 500 keV.

bounds. We first compared best-fit results for the  $\chi^2$  and C-stat distributions and overall we find improved constraints when using C-stat. Figure 3 shows the distributions of best-fit  $E_{\text{cut}}$  values for the absorbed power law model fit to the data for both  $\chi^2$  and C-stat. We observe that with the  $\chi^2$  statistic, a large number of sources have high energy cutoffs pegged at the upper limit of the model, leading to mean and median  $E_{\text{cut}}$  values that are skewed to higher energies. With C-stat, significantly fewer sources have best-fit coronal cutoff values at the upper limit of the model, producing average cutoffs that are lower and more closely resembling the true mean of the distribution, particularly since curvature in the spectrum at high energies associated with the coronal cutoff is not washed out, which can often be the case with the relatively wide energy bins necessary for  $\chi^2$  fitting.

We find full constraints on  $E_{\text{cut}}$  (both lower and upper limits) for 60 observations in our sample using C-stat, compared to 44 full  $E_{\text{cut}}$  constraints when performing spectral fitting with  $\chi^2$  for the absorbed power law model. For the PEXRAV model, we obtain full  $E_{\text{cut}}$  constraints for 91 observations with C-stat and 70 observations with  $\chi^2$  statistics. For the final XILLVERCP model, full constraints on  $kT_e$  are obtained for 79 observations with C-stat and 43 observations with  $\chi^2$ . In all cases, the number of full constraints on  $E_{\text{cut}}$  or  $kT_e$  is greater when applying the C-statistic compared to the

$\chi^2$  statistic. Furthermore, we note that while some individual AGN may have very high cutoff energies, e.g. Cen A (Fürst et al. 2016), generally average high energy cutoffs of the AGN population cannot exceed several hundred keV as this would otherwise overproduce the cosmic X-ray background above 100 keV (Gilli et al. 2007; Ananna et al. 2019).

In Figure 4 we present distributions of coronal cutoff energies using C-stat for the three spectral models considered in this work. Overall, we find good agreement between the different spectral models for the mean value of  $E_{\text{cut}}$ . We determine the mean value of  $E_{\text{cut}}$  or  $kT_e$  from the best-fit distributions presented in Figure 4 (purple). We do not include best-fit values of  $E_{\text{cut}}$  or  $kT_e$  that are pegged at the upper limit of the spectral model (500 keV, 1 MeV and 400 keV for models 1, 2 and 3 respectively) in our determination of mean values, as such values typically result from XSPEC being unable to determine error bounds from the data. For the XILLVERCP model, assuming a conversion factor for  $E_{\text{cut}} \sim 2\text{--}3 kT_e$  (Petrucci et al. 2001), the mean value of  $kT_e = 84 \pm 9$  keV is consistent with the mean value of  $E_{\text{cut}}$  derived for spectral models 1 and 2, which were found to be  $137 \pm 12$  keV and  $156 \pm 13$  keV respectively. Table 1 presents example spectral fit constraints and source properties for some select objects from our sample.

We generally find good agreement when comparing our  $E_{\text{cut}}$  or  $kT_e$  results to similar measurements for unobscured AGN reported in the literature. For example, Ricci et al. (2017) reported a median value of  $E_{\text{cut}} = 210 \pm 36$  keV for unobscured AGN from the *Swift*/BAT 70-month catalog, determined from broadband spectral fitting of *Swift*/BAT and *Suzaku* data. In recent work by Molina et al. (2019) which studied *NuSTAR* spectra for a small sample of 18 broad-lined AGN selected with *INTEGRAL*, a mean value of  $E_{\text{cut}} = 111 \pm 45$  keV was obtained for their sample, which is marginally consistent with our measurements given the large uncertainty.

#### 4.2. Relation between the High Energy Cutoff and Accretion Parameters

We next explore possible relations between the cutoff energy/temperature and fundamental accretion properties of the SMBH, such as Eddington ratio ( $L/L_{\text{Edd}}$ ) and mass of the SMBH ( $M_{\text{BH}}$ ). We adopt black hole mass estimates from the second data release of optical measurements from the BASS survey (DR2: Broad-Line Based Black Hole Mass Estimates and Biases from Obscuration, Mejía-Restrepo et al., submitted). In addition to broad-line measurements from optical spectra, black hole mass estimates from the BASS survey have been

compiled using several other techniques, such as stellar velocity dispersions, direct methods such as maser emission and reverberation mapping, and the  $M_{\text{BH}} - \sigma_*$  relation of Kormendy & Ho (2013). The Eddington luminosity  $L_{\text{Edd}}$  for pure H composition is given by:

$$L_{\text{Edd}} = \frac{4\pi GM_{\text{BH}}m_p c}{\sigma_T} \quad (2)$$

where  $G$  is the gravitational constant,  $c$  is the speed of light, and  $\sigma_T$  is the Thompson scattering cross section. We calculate the Eddington ratio  $L/L_{\text{Edd}}$  using the bolometric AGN luminosity, determined from the intrinsic X-ray luminosity in the 2–10 keV band, applying a bolometric correction factor of 20 to the 2–10 keV luminosity (Vasudevan & Fabian 2009).

Figure 5 presents the lower bound of  $E_{\text{cut}}$  or  $kT_e$  versus Eddington ratio for the three spectral models considered. Since our sample contains a large number of sources with either partial constraints or lower limits on the coronal cutoff energy, for consistency we examine the trend in the lower bounds of  $E_{\text{cut}}$  or  $kT_e$  across the entire sample. While our sample includes some strong constraints for bright AGN with long *NuSTAR* exposures, as noted in Baloković et al. (2020), for large sample statistics, such lower bound constraints are more informative than analysis of a small number of tightly constrained limits. Recently, Akylas & Georgantopoulos (2021) studied the coronal cutoffs in *Swift*/BAT-selected Sy 1 AGN using *NuSTAR* data, incorporating techniques similar to Baloković et al. (2020) that allow them to take the numerous lower limits on  $E_{\text{cut}}$  into account. Best-fit values of  $E_{\text{cut}}$  or  $kT_e$  obtained from spectral fitting with XSPEC can fluctuate between the upper and lower bounds with refitting, thus the lower bound presents a more robust constraint. We also note lower bounds on the cutoff energy that lie well outside the *NuSTAR* bandpass should be considered with due caution, due to uncertainties in spectral modeling combined with limitations in data quality for some sources. For example, Matt et al. (2015) found  $E_{\text{cut}} = 720^{+130}_{-190}$  keV when fitting the *NuSTAR* spectrum of NGC 5506 with a relativistic reflection model. However, Baloković et al. (2020) found  $E_{\text{cut}} = 110 \pm 10$  keV for NGC 5506 when fitting the same *NuSTAR* data with a slightly different spectral model. Despite the improved sensitivity of broadband spectra taken with *NuSTAR* and usage of more physically accurate reflection models, the extrapolation of Comptonization spectra to energies above the bandpass of *NuSTAR* presents large uncertainties and are overall difficult to predict above 100 keV (e.g., Niedźwiecki et al. 2019; Zdziarski et al. 2021).

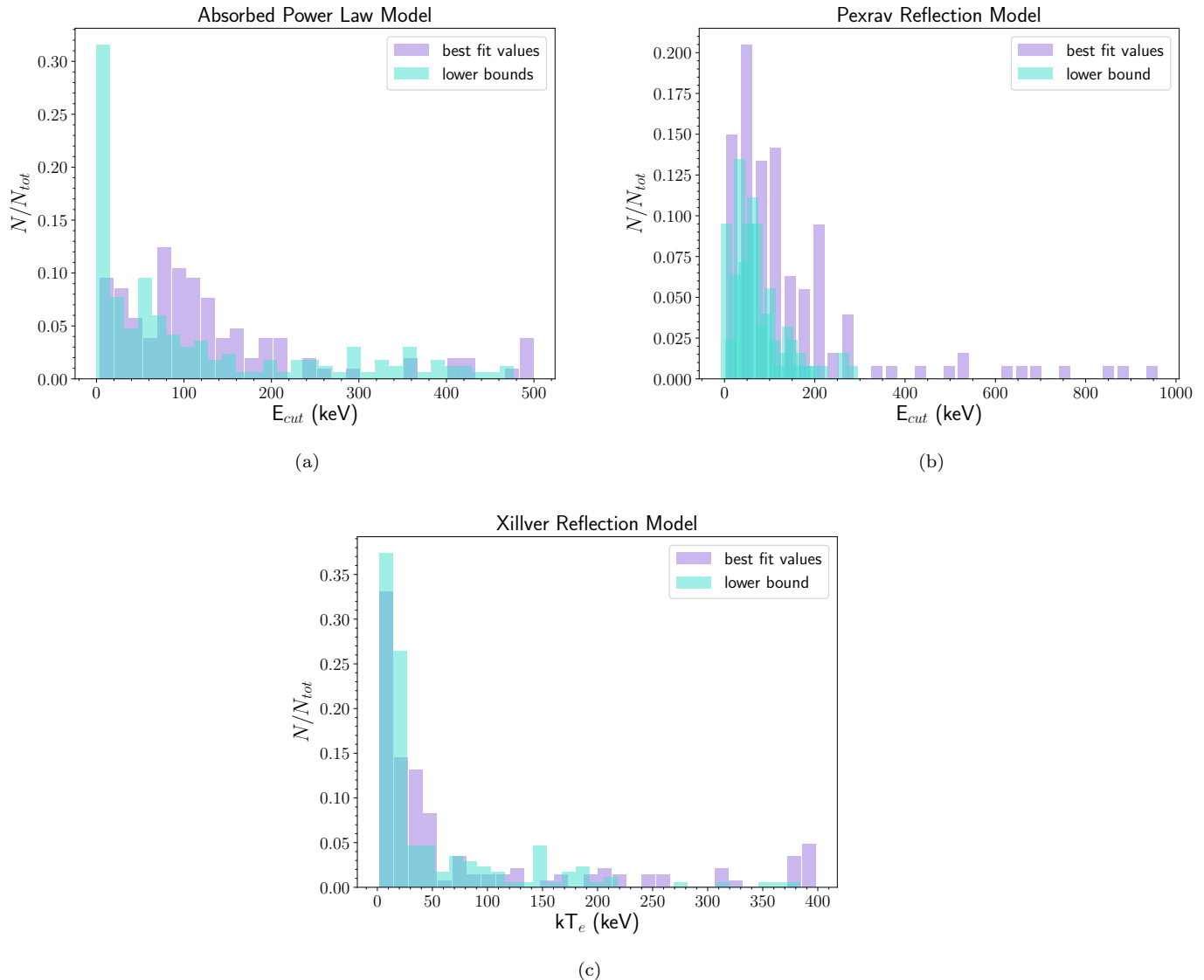


**Figure 4.** Distributions of the best-fit values and lower bounds of the high energy cutoff,  $E_{cut}$ , and coronal temperature,  $kT_e$ , for the different spectral models applied to the broadband X-ray data for our entire sample, using C-stat. Mean best-fit values of the coronal cutoff for the different spectral models, as determined from the purple histograms, are as follows: (a)  $E_{cut} = 137 \pm 12$  keV (b)  $E_{cut} = 156 \pm 13$  keV (c)  $kT_e = 84 \pm 9$  keV.

We do not find a significant correlation between the lower bound of the coronal cutoff and Eddington ratio for the full sample, with p-values exceeding 1 % when applying a Spearman rank correlation test to both individual points and binned data. We also investigated the dependence of the coronal cutoff on the mass of the AGN SMBH ( $M_{BH}$ ). Figure 6 shows the results for different spectral models. While we find a declining trend in the mean lower bound of  $E_{cut}$  with  $M_{BH}$  for the absorbed power law model, with a p-value of 0.004%, we do not find any statistically significant correlation for the two reflection models (p-value > 10%), which more

accurately characterize the AGN emission compared to the simple power law fit.

Comparing our results with similar studies of coronal parameters by Ricci et al. (2018) using pre-*NuSTAR* broadband X-ray data, we find some differences. Ricci et al. (2018) find a negative trend in the median value of  $E_{cut}$  with Eddington ratio for their sample of 211 unobscured AGN, including lower limits. However no significant correlation is found between  $E_{cut}$  and Eddington ratio when lower limits are ignored in their sample. While they observe a possible trend between  $E_{cut}$  and  $M_{BH}$ , such a correlation disappears when dividing the

**Table 1.** Redshifts, black hole masses and best-fit spectral parameters from fitting broadband X-ray data for select sources from our sample of *Swift*/BAT-selected Sy1s

Source	Redshift	$\log(M_{\text{BH}}/M_{\odot})^A$	$\Gamma$	$E_{\text{cut}}$ (keV)	$kT_e$ (keV)	C-stat/dof	Model <sup>B</sup>
Fairall 1203	0.058	8.20	$1.24^{+0.15}_{-0.17}$	$42^{+51}_{-16}$	-	1052/1192	1
			$1.45^{+0.23}_{-0.19}$	$\geq 45$	-	186/247	2
			$1.56^{+0.05}_{-0.04}$	-	$15^{+39}_{-4}$	1043.5/1189	3
IC 4329A	0.016	7.81	$1.69^{+0.004}_{-0.01}$	$\geq 394$	-	4955/4179	1
			$1.72 \pm 0.01$	$170^{+23}_{-18}$	-	2698/2706	2
			$1.77^{+0.01}_{-0.004}$	-	$82^{+16}_{-7}$	4275.7/4210	3
MCG-3-4-72	0.046	7.09	$1.73 \pm 0.05$	$117^{+223}_{-48}$	-	1554/1642	1
			$1.95 \pm 0.06$	$123^{+596}_{-59}$	-	748.5/749	2
			$1.73^{+0.04}_{-0.05}$	-	$15^{+23}_{-4}$	1537/1654	3
Mrk 1148	0.064	8.01	$1.73^{+0.05}_{-0.04}$	$81^{+59}_{-18}$	-	2138/2262	1
			$1.89 \pm 0.04$	$\geq 85$	-	1477/1633	2
			$1.78^{+0.04}_{-0.03}$	-	$\geq 18$	2167.5/2290	3
RBS 542	0.104	7.89	$1.61 \pm 0.02$	$74^{+14}_{-10}$	-	3389.8/3251	1
			$1.64 \pm 0.03$	$49^{+7}_{-5}$	-	1658/1570	2
			$1.70^{+0.03}_{-0.02}$	-	$\geq 16$	3253/3257	3

NOTE—Information presented in this table is available for our full sample in machine-readable form.

<sup>A</sup> Reference: Mejía-Restrepo et al., submitted (BASS XXII DR2: Broad-line based black hole mass estimates and biases from obscuration).

<sup>B</sup> Applied XSPEC models: (1)  $c_{\text{inss}} \times \text{TBABS} \times \text{ZPHABS} \times \text{CUTOFFPL}$

(2)  $c_{\text{inss}} \times \text{TBABS} \times \text{ZPHABS} \times (\text{CUTOFFPL} + \text{ZGAUSS} + \text{PEXRAV})$

(3)  $c_{\text{inss}} \times \text{TBABS} \times \text{ZPHABS} \times (\text{XILLVERCP} + \text{ZGAUSS})$

sources into bins of different Eddington ratio. Tortosa et al. (2018) studied coronal parameters in a sample of 19 *Swift*/BAT-selected Seyfert 1 galaxies observed with *NuSTAR*, and found no correlation between the high energy cutoff and SMBH mass or Eddington ratio. In another study, Molina et al. (2019) examined X-ray spectra of 18 broad-lined AGN selected with *INTEGRAL* and observed with *NuSTAR*. They found no correlation between the high energy coronal cutoff and Eddington ratio. In a more recent study by Hinkle & Mushotzky (2021), which examined coronal parameters in a sample of 33 *Swift*/BAT-selected Sy1 and Sy2 AGN observed with *NuSTAR* and *XMM-Newton*, no strong correlation was found between cutoff energy and SMBH mass or Eddington ratio. Therefore, we demonstrate that when fitting high quality broadband X-ray spectra obtained with *NuSTAR* for large samples of AGN, we do not find a strong correlation between the coronal cutoff and AGN accretion parameters such as Eddington ratio and SMBH mass.

#### 4.3. The $\Gamma - L/L_{\text{Edd}}$ Relation

Next, we investigate the relationship between the X-ray photon index and Eddington ratio, hereafter referred

to as the  $\Gamma - L/L_{\text{Edd}}$  relation. Numerous studies report a positive linear correlation between these two parameters, of the form

$$\Gamma = \Psi \log\left(\frac{L}{L_{\text{Edd}}}\right) + \omega. \quad (3)$$

Early studies of individual sources and small samples of AGN hinted at a correlation between  $\Gamma$  and  $L_{\text{Edd}}$  (e.g., Pounds et al. 1995; Brandt et al. 1997), though such studies probed a very limited range of AGN luminosities. Studies covering a wider range of luminosities and redshifts such as Shemmer et al. (2006, 2008) and Brightman et al. (2013) identified a statistically significant correlation between  $\Gamma$  and  $L_{\text{Edd}}$ , with a slope  $\Psi \sim 0.3$ . However, Sobolewska & Papadakis (2009) performed detailed spectral analysis of 10 *RXTE*-observed AGN and found  $\Psi$  to vary from object to object, with a flatter average slope  $\Psi = 0.08$ . Yang et al. (2015) constructed a large sample of AGN and black hole binaries covering a wide luminosity range, and found  $\Gamma$  to be constant at very low luminosities, but varied from being positively and negatively correlated over certain luminosity ranges. Recent studies by Trakhtenbrot et al. (2017) which examined the  $\Gamma - L/L_{\text{Edd}}$  relation for 228

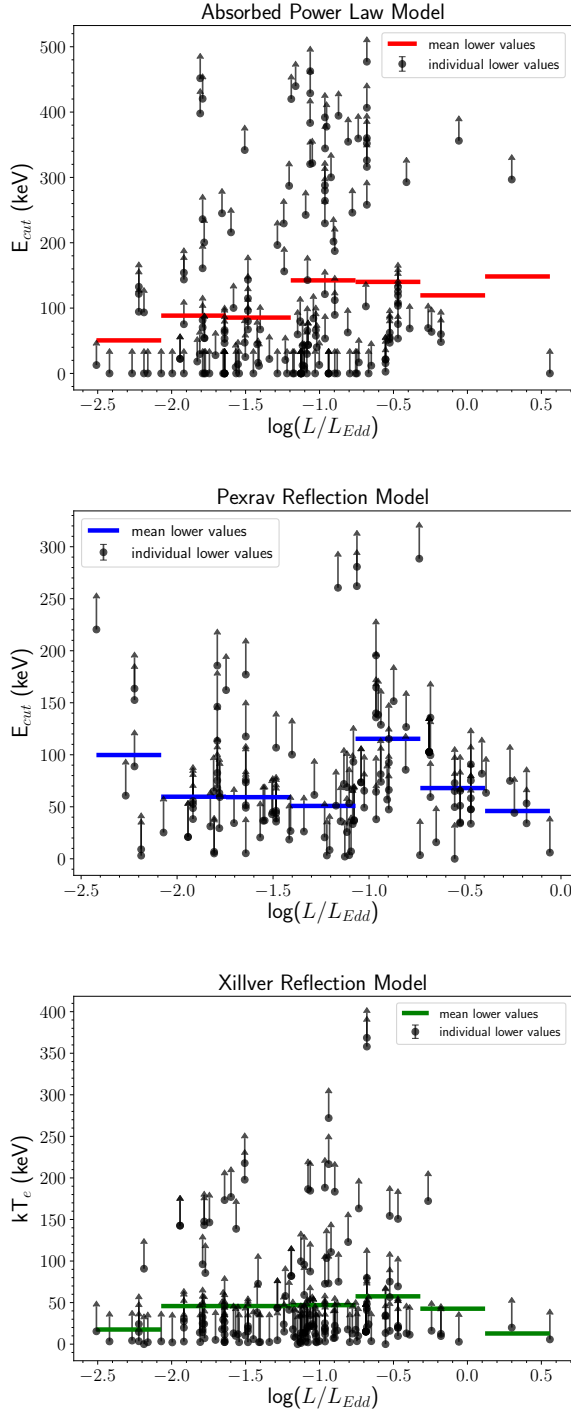


**Figure 5.** Lower bounds of  $E_{\text{cut}}$  and  $kT_e$  versus the Eddington ratio  $L/L_{\text{Edd}}$  for different X-ray spectral models applied to our entire sample, using C-stat. Solid horizontal lines represent mean values of  $E_{\text{cut}}$  or  $kT_e$  for different intervals of  $L/L_{\text{Edd}}$ .

Swift/BAT AGN, have also reported flatter slopes ( $\Psi \sim 0.15$ ), with overall large scatter in the relation. Further-

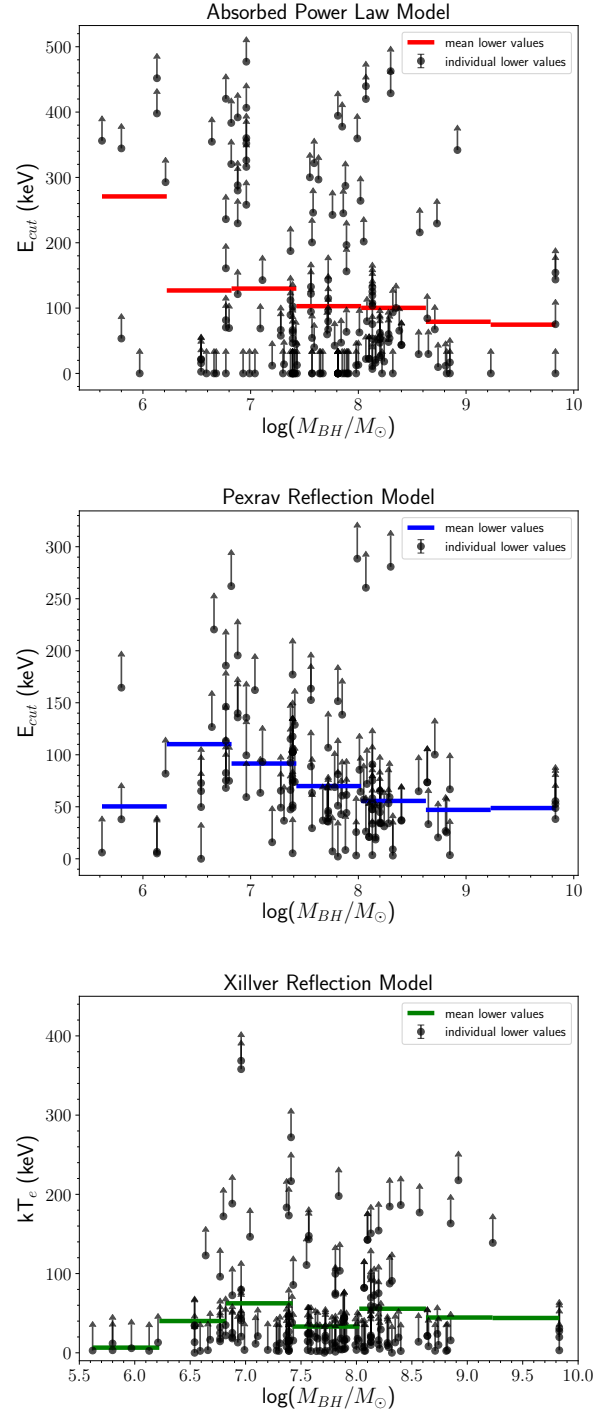


**Figure 6.** Lower bounds of  $E_{\text{cut}}$  and  $kT_e$  versus SMBH mass  $M_{\text{BH}}$  for different X-ray spectral models applied to our entire sample, using C-stat. Solid horizontal lines represent mean values of  $E_{\text{cut}}$  or  $kT_e$  for different intervals of  $M_{\text{BH}}$ .

more, the authors found no evidence for a  $\Gamma - L/L_{\text{Edd}}$  correlation for subsets of AGN with reliable, direct BH mass estimates. Ricci et al. (2013) also found a similarly

flat slope ( $\Psi = 0.12$ ) for their sample of 36 *Chandra*-observed AGN. In [Trakhtenbrot et al. \(2017\)](#), the authors only recover the steeper slope consistent with earlier studies ( $\Psi \sim 0.3$ ) when applying a simple power law model fit to the subset of broad-lined AGN in their sample. These results demonstrate that the  $\Gamma - L/L_{\text{Edd}}$  relation may not be robust or universal, with the strength of the correlation varying with choice of sample, luminosity ranges of the sample, energy range of X-ray data used in analysis, and type of X-ray spectral model used in determining  $\Gamma$ .

In our work, we examined the  $\Gamma - L/L_{\text{Edd}}$  relation for our full sample for all three X-ray spectral models used in our analysis. We also investigated whether there was a dependence of the slope of the relation on the type of X-ray spectral model fitted to the broadband data. We present our results for the  $\Gamma - L/L_{\text{Edd}}$  relation in [Figure 7](#), showing  $\Gamma$  values for the XILLVER reflection model, which most accurately characterizes the AGN X-ray emission. Overall, we find considerable scatter and no strong trend between  $\Gamma$  and  $L_{\text{Edd}}$  for all spectral models that we applied. Applying a formal Spearman rank test confirmed the absence of a statistically significant correlation, with correlation coefficients less than 0.25 and p-values exceeding 0.2%. We find no strong correlation when dividing the data into bins of Eddington ratio (purple lines in [Figure 7](#)). When applying a simple linear regression fit to the data for each X-ray spectral model, we obtain very flat slopes:  $\Psi \sim 0.03 - 0.06$ . Comparing to the literature, our slopes for the  $\Gamma - L/L_{\text{Edd}}$  relation are much flatter than previously reported results, as we find little evidence for a correlation between  $\Gamma$  and  $L_{\text{Edd}}$ . We conclude that when analyzing a large, unbiased sample of unobscured AGN with high sensitivity broadband X-ray spectral data, we do not find robust evidence for a  $\Gamma - L/L_{\text{Edd}}$  correlation and caution on the usage of such a relation to derive estimates of  $L_{\text{Edd}}$  or  $M_{\text{BH}}$ .

#### 4.4. Location of Sources in the Compactness–Temperature Plane

Using our constraints on the coronal temperature, we constructed a compactness–temperature ( $l - \theta$ ) diagram using sources from our sample.  $\theta$  is defined to be a dimensionless parameter for coronal temperature:  $\theta = kT_e/m_e c^2$ . In constructing the  $l - \theta$  plane, we use  $kT_e$  values obtained from the XILLVER spectral model fit to the X-ray data. This eliminates the uncertainty in determining  $\theta$  from  $E_{\text{cut}}$  values, since the conversion from  $E_{\text{cut}}$  to  $kT_e$  varies depending on the optical depth of the corona ([Petrucci et al. 2001](#)), which can vary from source to source. In determining values of  $l$ , we assume a con-

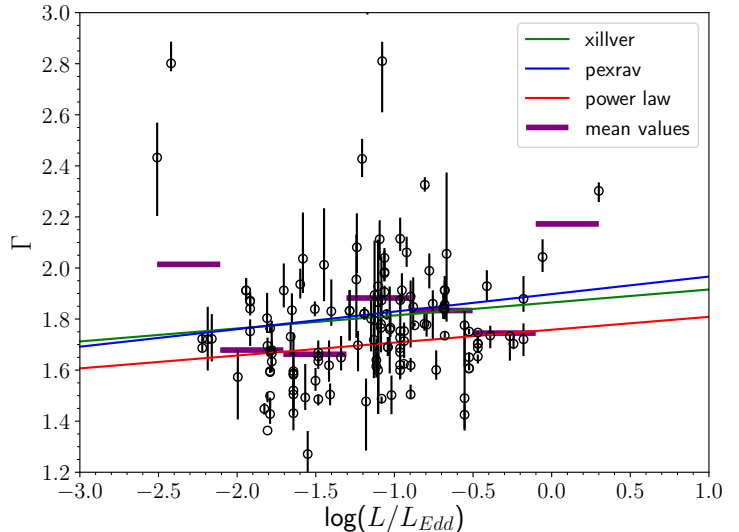


**Figure 7.** The  $\Gamma - L/L_{\text{Edd}}$  relation for our full sample. Solid lines show linear fits to the data for the three different X-ray spectral models applied in this work. Marked in purple are mean values of  $\Gamma$  for different bins of Eddington ratio for the XILLVER reflection model.

servative value of  $10R_g$  for the coronal radius ([Fabian et al. 2015](#)).

[Figure 8](#) presents compactness–temperature diagrams for the AGN in our sample for which black hole mass estimates are available. We plot several pair production lines corresponding to different coronal geometries. Treating the corona as an isolated cloud, [Svensson \(1984\)](#) calculated the pair production line to have an analytical form  $l \sim 10\theta^{5/2}e^{1/\theta}$ , which is shown in solid cyan in our  $l - \theta$  plots. We also mark pair production lines for a slab and hemispherical corona located above a reflecting accretion disk computed from [Stern et al. \(1995\)](#) (black and purple lines respectively in [Figure 8](#)). In the top panel of [Figure 8](#) the dashed lines correspond to the boundaries where electron–electron (black) and electron–proton (green) processes dominate over Compton cooling ([Ghisellini et al. 1993](#); [Fabian 1994](#)). The lower plot shows the distribution of sources on the  $l - \theta$  plane individually color coded by black hole mass.

These  $l - \theta$  measurements for our large sample of *NuSTAR*-observed AGN generally show sources to be widely distributed in both temperature and radiative compactness, in contrast to previous measurements for smaller samples of AGN where sources appeared to cluster near the pair production lines (e.g., [Fabian et al. 2015](#); [Kamraj et al. 2018](#)). The results from [Ricci et al. \(2018\)](#), which mapped the  $l - \theta$  plane for 211 unob-

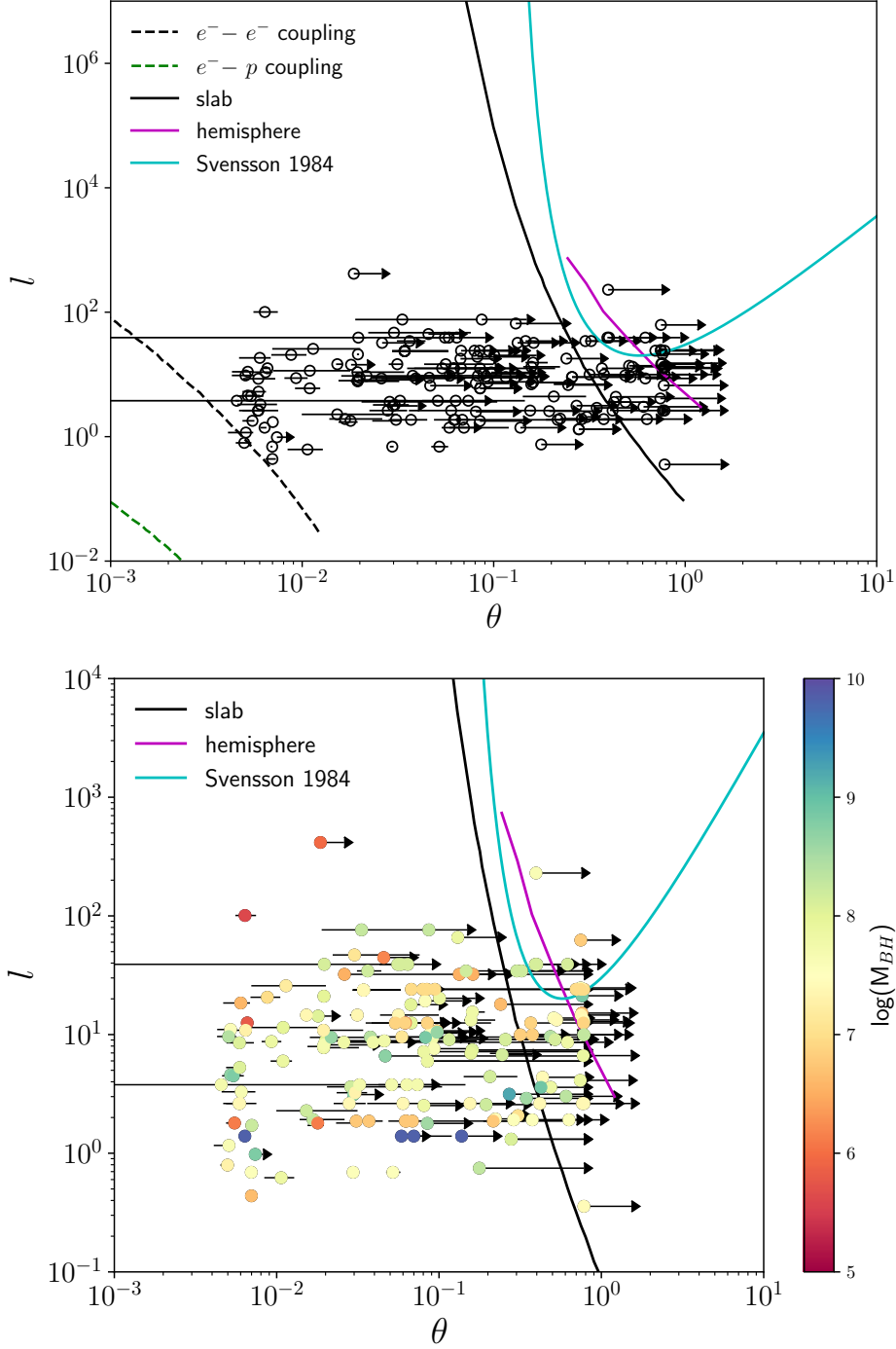


**Figure 8.** Compactness-Temperature ( $l-\theta$ ) diagrams for our full sample, with  $\theta$  determined using  $kT_e$  values from the XILLVER model fit to data. Solid lines correspond to pair production lines for different coronal geometries. The dashed lines in the top panel correspond to boundaries where regions are dominated by electron-electron and electron-proton coupling processes. Data points in the bottom panel plot are color coded by SMBH mass.

scured *Swift*/BAT AGN, show a distribution of individual sources fairly similar to our results.

In general, the existence of AGN with low coronal temperatures is rather enigmatic, as the mechanisms behind coronal cooling in such sources are not well under-

stood. Identification of AGN with low coronal temperatures is not uncommon, with findings of high energy cutoffs within the *NuSTAR* band reported in the literature in recent years (e.g., Kara et al. 2017; Xu et al. 2017; Kamraj et al. 2019). Various theories have been

proposed for possible cooling mechanisms to account for such low temperatures within the corona. Weak coronal heating mechanisms are a possibility, considering that it has been a longstanding open problem of supplying energy to the corona when it is established that the cooling timescale is shorter than the light crossing timescale (e.g., Ghisellini et al. 1993; Merloni & Fabian 2001). Low coronal temperatures could also be produced from a high optical depth within the corona. For optical depths exceeding unity, multiple inverse Compton scatterings of photons originating from the accretion disk could lead to effective coronal cooling (Kara et al. 2017). However, we have thus far assumed the corona is homogeneous, fully thermal, and at a single temperature, whereas in reality the corona is a dynamic structure and can have a range of temperatures (Fabian et al. 2015). It is possible that the corona is a hybrid plasma, containing both thermal and non-thermal particles (e.g., Zdziarski et al. 1993a; Ghisellini et al. 1993). Fabian et al. (2017) have shown through hybrid plasma simulations that a small fraction of non-thermal electrons with energies above 1 MeV can reduce the temperature of the corona, as electron-positron pairs redistribute their energy and reduce the mean energy per particle.

Our  $l - \theta$  measurements improve over previously reported studies by combining both a large sample size of AGN with high quality *NuSTAR* broadband X-ray data with improved spectral modeling for determination of coronal temperatures. By using the XILLVERCP spectral model, we obtain more accurate estimates of  $kT_e$ , since the high energy turnover in the intrinsic continuum is modeled as a Comptonized spectrum instead of the common exponential power law cutoff. Past works such as Zdziarski et al. (1993b) and Fabian et al. (2015) have shown that a simple exponential cutoff approximation produces a slower break in the X-ray spectrum compared to a Comptonized continuum, which retains a power law shape to higher X-ray energies before more rapidly turning over. Thus, an exponential cutoff approximation can lead to overestimates of the coronal temperature.

We note that higher order effects can affect the precise location of sources on the  $l - \theta$  plane. Most notably, general relativistic effects such as gravitational redshift and light bending can affect estimates of  $l$  and  $\theta$ . For example, light bending can boost intrinsic values of  $l$  and enhance Compton cooling, thereby moving pair lines to lower  $\theta$ . However, such corrections are highly dependent on properties such as disk inclination and coronal geometry, both of which are highly uncertain. Hence, we do not attempt to model general relativistic effects in this

work due to the large uncertainties associated with such corrections.

#### 4.5. Optical Depth of the Coronal Plasma

In this final section we report on the investigation of other AGN parameters derived from broadband X-ray spectral fit results for our full sample. Specifically, we focus on determining the optical depth of the plasma in the corona ( $\tau$ ) and its relation to the Eddington ratio. The optical depth is not a parameter that is directly determined from X-ray spectral fitting, but it can be derived from  $\Gamma$  and  $kT_e$  according to the following equation given in Zdziarski et al. (1996) for a spherical corona and formally valid for  $\tau \gtrsim 1$ :

$$\Gamma = \sqrt{\frac{9}{4} + \frac{511 \text{ keV}}{\tau kT_e(1 + \tau/3)}} - \frac{1}{2}. \quad (4)$$

We use best-fit values of  $kT_e$  found from the XILLVERCP reflection model to solve for  $\tau$  according to Equation 4. We find that the median and mean optical depths for our entire sample are  $\tau = 3.04 \pm 1.73$  and  $\tau = 4.84 \pm 1.80$  respectively. We note that a large number of sources in our sample have only a lower limit on  $kT_e$  and so the values of  $\tau$  presented in this work should be viewed as upper limits. We also note that parameter degeneracies, particularly in the  $kT_e - \Gamma$  plane, can lead to very high values of  $\tau$ . Spectral fits that produce very low values of  $kT_e$  accompanied by low values of  $\Gamma$  do not correspond to physically realistic conditions within the coronal plasma (e.g., Stern et al. 1995; Poutanen & Svensson 1996). In Figure 9 we show best-fit values of  $kT_e$  and  $\Gamma$  along with curves of constant  $\tau$  defined using equation 4. We observe that while there is some degree of degeneracy present in the  $kT_e - \Gamma$  plane, the majority of sources lie above the line roughly corresponding to the mean value of  $\tau$  for our sample.

For sources with full constraints on  $kT_e$ , we performed Monte Carlo sampling as a rough estimate of the uncertainty in derived values of  $\tau$ . We drew 1000 random samples of  $kT_e$  and  $\Gamma$ , assuming a mean and variance of the random sample taken from the observed respective distributions. We found no difference in the distributions of  $\tau$  determined from the randomly sampled values of  $kT_e$  and  $\Gamma$  when assuming different underlying types of distribution (e.g. Gaussian vs. Poissonian).

In Figure 10 we present results for  $\tau$  against the Eddington ratio, with each source color-coded by its best-fit value of  $kT_e$ . We do not find a statistically significant correlation between  $\tau$  and  $L/L_{\text{Edd}}$  for individual data points or when binning the data by  $L/L_{\text{Edd}}$ , similar to results from Ricci et al. (2018). From Figure 10

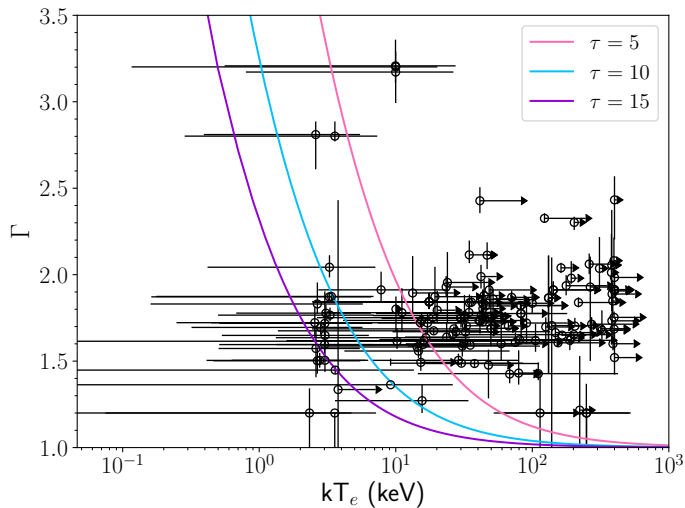


**Figure 9.**  $kT_e$  and  $\Gamma$  values obtained from the XILLVER spectral model fit to the data. Solid colored lines correspond to curves of constant coronal plasma optical depth  $\tau$ , according to Equation 4.

we also observe a trend of increasing optical depth with decreasing coronal temperature. Tortosa et al. (2018) also found a negative correlation between the plasma optical depth and coronal temperature for their sample of 19 *NuSTAR*-observed Seyfert 1 galaxies. This observed trend in  $\tau$  with  $L/L_{\text{Edd}}$  supports the hypothesis mentioned in Section 4.4 for low temperature coronae possibly possessing high optical depths, thus enhancing coronal cooling.

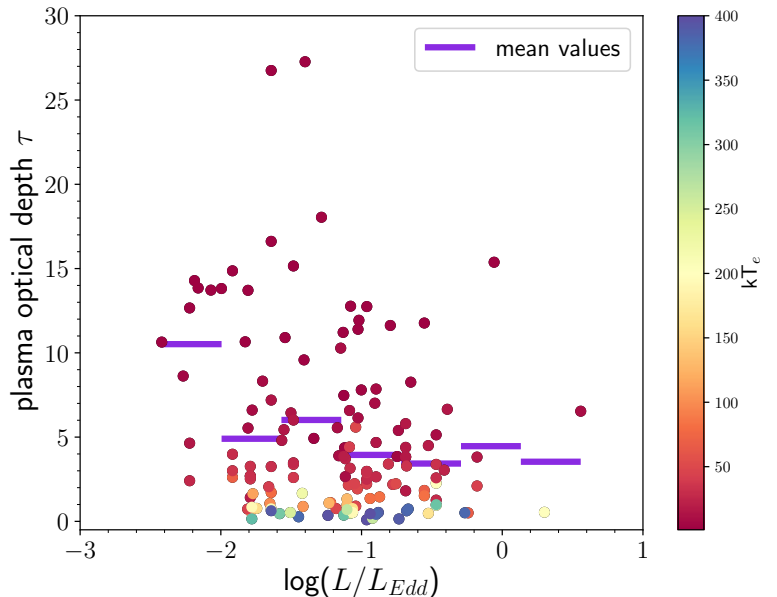


**Figure 10.** Coronal plasma optical depth  $\tau$  versus the Eddington ratio  $L/L_{\text{Edd}}$  for our entire sample. Optical depth was derived from  $kT_e$  and  $\Gamma$  values obtained from the XILLVER spectral model fit to the data. Horizontal purple lines correspond to mean values of  $\tau$  for different bins of Eddington ratio. Data points are color coded by their corresponding  $kT_e$  value found from X-ray spectral fitting.

## 5. SUMMARY

In this work, we have compiled a large sample of Seyfert 1 AGN with high quality broadband X-ray spectra taken with the *NuSTAR* observatory and studied fundamental properties of the coronal plasma that powers the continuum X-ray emission in AGN. We performed detailed broadband X-ray spectral modeling for all sources in our sample from which we obtained constraints on the temperature of the corona. From fitting a more physically accurate advanced reflection model, we find the mean coronal temperature to be  $kT_e = 84 \pm 9$  keV, which is generally consistent with other measurements of high energy cutoffs for unobscured AGN reported in the literature.

When investigating the relationship between the coronal temperature and accretion parameters such as the Eddington ratio and AGN SMBH mass, we do not find any strong correlations. We also examined the well-known  $\Gamma - L/L_{\text{Edd}}$  relation, and found no statistically significant correlation, with little variation in the slope of the relation with the choice of X-ray spectral model used to determine  $\Gamma$ . We thus caution on the use of such relations previously presented in the literature to derive distributions of  $L/L_{\text{Edd}}$  or  $M_{\text{BH}}$ .

We studied the distribution of sources in our sample across the compactness-temperature plane and find AGN to span a wide range of coronal temperatures and are not strictly confined to the boundary lines corresponding to runaway pair production. A number of sources appear to have fairly low coronal temperatures, which may arise from large optical depths of the coronal plasma, as we observe the optical depth of sources in our sample to increase with decreasing values of the coronal temperature. Another possibility is that the corona is a hybrid plasma system, where the presence of a population of non-thermal electrons can act to reduce the temperature of the plasma. Future studies that can apply advanced hybrid plasma models to high quality broadband AGN X-ray spectral observations performed with *NuSTAR* or concept X-ray missions such as *HEXP* (Madsen et al. 2019), may be able to robustly test the possibility of such a physical scenario producing a low temperature corona.

*Facilities:* *NuSTAR*, *Swift*, *XMM-Newton*, *Palomar Hale (DBSP)*

*Software:* TBABS (Wilms et al. 2000), PEXRAV (Magdziarz & Zdziarski 1995), NTHCOMP (Zdziarski et al. 1996), XILLVERCP (García & Kallman 2010), NuSTARDAS (v2.17.1), HEASOFT (v6.24), XMM SAS (v16.1.0), XSPEC (v12.8.2), Astropy (Astropy Collaboration et al. 2013, 2018), NumPy, Matplotlib (Hunter 2007)

1 We have made use of data from the *NuSTAR* mission,  
 2 a project led by the California Institute of Technology,  
 3 managed by the Jet Propulsion Laboratory, and funded  
 4 by the National Aeronautics and Space Administration.  
 5 We thank the *NuSTAR* Operations, Software and Cali-  
 6 bration teams for support with the execution and anal-  
 7 ysis of these observations. This research has made use  
 8 of the following resources: *NuSTAR* Data Analysis Soft-  
 9 ware (NuSTARDAS) jointly developed by the ASI Sci-  
 10 ence Data Center (ASDC, Italy) and the California In-  
 11 stitute of Technology (USA); online *Swift* data process-  
 12 ing services provided by the SSC; the High Energy  
 13 Astrophysics Science Archive Research Center Online  
 14 Service, provided by the NASA/Goddard Space Flight  
 15 Center; NASA’s Astrophysics Data System; *Astropy*, a  
 16 community-developed core Python package for Astron-  
 17 omy (Astropy Collaboration et al. 2013, 2018). Some  
 18 of the optical spectra used for determining black hole  
 19 masses used in this work were taken with the Double-  
 20 spec (DBSP) instrument at Palomar via Yale (PI M.  
 21 Powell, 2017-2019, 16 nights) as well as Caltech (PI F.  
 22 Harrison) and JPL (PI D. Stern) from programs from  
 23 2013-2020.

24 M. Baloković acknowledges support from the Black  
 25 Hole Initiative at Harvard University, which is funded  
 26 in part by the Gordon and Betty Moore Foundation  
 27 (grant GBMF8273) and in part by the John Temple-  
 28 ton Foundation, as well as support from the YCAA  
 29 Prize Postdoctoral Fellowship. M.K. acknowledges sup-  
 30 port from NASA through ADAP award NNH16CT03C.  
 31 K.O. acknowledges support from the National Research  
 32 Foundation of Korea (NRF-2020R1C1C1005462). C.R.  
 33 acknowledges support from the CONICYT+PAI Convo-  
 34 catoria Nacional subvencion a instalacion en la academia  
 35 convocatoria año 2017 PAI77170080.

## REFERENCES

- Akylas, A., & Georgantopoulos, I. 2021, *A&A*, arXiv:2108.11337
- Ananna, T. T., Treister, E., Urry, C. M., et al. 2019, *ApJ*, 871, 240
- Arnaud, K. 1996, in *ASP Conf. Series*, Vol. 101, *Astronomical Data Analysis Software and Systems*, ed. G. H. Jacoby & J. Barnes, 17
- Astropy Collaboration, Robitaille, T. P., Tollerud, E. J., et al. 2013, *A&A*, 558, A33
- Astropy Collaboration, Price-Whelan, A. M., Sipőcz, B. M., et al. 2018, *AJ*, 156, 123
- Ballantyne, D. R., Bollenbacher, J. M., Brenneman, L. W., et al. 2014, *ApJ*, 794, 62
- Baloković, M., Matt, G., Harrison, F. A., et al. 2015, *ApJ*, 800, 62
- Baloković, M., Harrison, F. A., Madejski, G., et al. 2020, *ApJ*, 905, 41
- Baumgartner, W. H., Tueller, J., Markwardt, C. B., et al. 2013, *ApJS*, 207, 19
- Beckmann, V., Soldi, S., Ricci, C., et al. 2009, *A&A*, 505, 417
- Brandt, W. N., Mathur, S., & Elvis, M. 1997, *MNRAS*, 285, L25
- Brenneman, L. W., Madejski, G., Fuerst, F., et al. 2014, *ApJ*, 781, 83
- Brightman, M., Silverman, J. D., Mainieri, V., et al. 2013, *MNRAS*, 433, 2485
- Burrows, D. N., Hill, J. E., Nousek, J. A., et al. 2005, *SSRv*, 120, 165
- Cash, W. 1979, *ApJ*, 228, 939
- Chartas, G., Rhea, C., Kochanek, C., et al. 2016, *Astronomische Nachrichten*, 337, 356
- Dadina, M. 2007, *A&A*, 461, 1209
- De Marco, B., Ponti, G., Cappi, M., et al. 2013, *MNRAS*, 431, 2441
- Evans, P. A., Beardmore, A. P., Page, K. L., et al. 2009, *MNRAS*, 397, 1177
- Fabian, A. C. 1994, *ApJS*, 92, 555
- Fabian, A. C., Lohfink, A., Belmont, R., Malzac, J., & Coppi, P. 2017, *MNRAS*, 467, 2566
- Fabian, A. C., Lohfink, A., Kara, E., et al. 2015, *MNRAS*, 451, 4375
- Fabian, A. C., Zoghbi, A., Ross, R. R., et al. 2009, *Nature*, 459, 540
- Fürst, F., Müller, C., Madsen, K. K., et al. 2016, *ApJ*, 819, 150
- Gabriel, C., Denby, M., Fyfe, D. J., et al. 2004, in *Astronomical Society of the Pacific Conference Series*, Vol. 314, *Astronomical Data Analysis Software and Systems (ADASS) XIII*, ed. F. Ochsenbein, M. G. Allen, & D. Egret, 759
- García, J., & Kallman, T. R. 2010, *ApJ*, 718, 695
- García, J., Dauser, T., Lohfink, A., et al. 2014, *ApJ*, 782, 76
- Gehrels, N., Chincarini, G., Giommi, P., et al. 2004, *ApJ*, 611, 1005
- Ghisellini, G., Haardt, F., & Fabian, A. C. 1993, *MNRAS*, 263
- Gilli, R., Comastri, A., & Hasinger, G. 2007, *A&A*, 463, 79
- Guilbert, P. W., Fabian, A. C., & Rees, M. J. 1983, *MNRAS*, 205, 593
- Haardt, F., & Maraschi, L. 1993, *ApJ*, 413, 507
- Harrison, F. A., Craig, W. W., Christensen, F. E., et al. 2013, *ApJ*, 770, 103
- Hinkle, J. T., & Mushotzky, R. 2021, *MNRAS*, 506, 4960
- Hunter, J. D. 2007, *Computing in Science and Engineering*, 9, 90
- Jansen, F., Lumb, D., Altieri, B., et al. 2001, *A&A*, 365, L1
- Kaastra, J. S. 2017, *A&A*, 605, A51
- Kalberla, P. M. W., Burton, W. B., Hartmann, D., et al. 2005, *A&A*, 440, 775
- Kamraj, N., Harrison, F. A., Baloković, M., Lohfink, A., & Brightman, M. 2018, *ApJ*, 866, 124
- Kamraj, N., Baloković, M., Brightman, M., et al. 2019, *ApJ*, 887, 255
- Kara, E., García, J. A., Lohfink, A., et al. 2017, *MNRAS*, 468, 3489
- Kormendy, J., & Ho, L. C. 2013, *ARA&A*, 51, 511
- Koss, M., Trakhtenbrot, B., Ricci, C., et al. 2017, *ApJ*, 850, 74
- Lubiński, P., Beckmann, V., Gibaud, L., et al. 2016, *MNRAS*, 458, 2454
- Madsen, K., Hickox, R., Bachetti, M., et al. 2019, in *Bulletin of the American Astronomical Society*, Vol. 51, 166
- Magdziarz, P., & Zdziarski, A. A. 1995, *MNRAS*, 273, 837
- Malizia, A., Molina, M., Bassani, L., et al. 2014, *ApJL*, 782, L25
- Matt, G., Baloković, M., Marinucci, A., et al. 2015, *MNRAS*, 447, 3029
- McHardy, I. M., Gunn, K. F., Uttley, P., & Goad, M. R. 2005, *MNRAS*, 359, 1469
- Merloni, A., & Fabian, A. C. 2001, *MNRAS*, 321, 549
- Molina, M., Malizia, A., Bassani, L., et al. 2019, *MNRAS*, 484, 2735

- Nicastro, F., Piro, L., De Rosa, A., et al. 2000, *ApJ*, 536, 718
- Niedźwiecki, A., Szanecki, M., & Zdziarski, A. A. 2019, *MNRAS*, 485, 2942
- Oh, K., Koss, M., Markwardt, C. B., et al. 2018, *ApJS*, 235, 4
- Osterbrock, D. E. 1981, *ApJ*, 249, 462
- Perri, M., Puccetti, S., Spagnuolo, N., et al. 2017, *The NuSTAR Data Analysis Software Guide v1.7*
- Petrucci, P. O., Haardt, F., Maraschi, L., et al. 2001, *ApJ*, 556, 716
- Pounds, K. A., Done, C., & Osborne, J. P. 1995, *MNRAS*, 277, L5
- Poutanen, J., & Svensson, R. 1996, *ApJ*, 470, 249
- Ricci, C., Paltani, S., Ueda, Y., & Awaki, H. 2013, *MNRAS*, 435, 1840
- Ricci, C., Walter, R., Courvoisier, T. J. L., & Paltani, S. 2011, *A&A*, 532, A102
- Ricci, C., Trakhtenbrot, B., Koss, M. J., et al. 2017, *ApJS*, 233, 17
- Ricci, C., Ho, L. C., Fabian, A. C., et al. 2018, *MNRAS*, 480, 1819
- Rothschild, R. E., Mushotzky, F. R., Baity, W. A., et al. 1983, *ApJ*, 269, 423
- Shemmer, O., Brandt, W. N., Netzer, H., Maiolino, R., & Kaspi, S. 2006, *ApJL*, 646, L29
- . 2008, *ApJ*, 682, 81
- Sobolewska, M. A., & Papadakis, I. E. 2009, *MNRAS*, 399, 1597
- Stern, B. E., Poutanen, J., Svensson, R., Sikora, M., & Begelman, M. C. 1995, *ApJL*, 449, L13
- Strüder, L., Briel, U., Dennerl, K., et al. 2001, *A&A*, 365, L18
- Svensson, R. 1984, *MNRAS*, 209, 175
- Tortosa, A., Bianchi, S., Marinucci, A., Matt, G., & Petrucci, P. O. 2018, *A&A*, 614, A37
- Trakhtenbrot, B., Ricci, C., Koss, M. J., et al. 2017, *MNRAS*, 470, 800
- Uttley, P., Cackett, E. M., Fabian, A. C., Kara, E., & Wilkins, D. R. 2014, *Astronomy and Astrophysics Review*, 22, 72
- Vasudevan, R. V., & Fabian, A. C. 2009, *MNRAS*, 392, 1124
- Verner, D. A., Ferland, G. J., Korista, K. T., & Yakovlev, D. G. 1996, *ApJ*, 465, 487
- Wilms, J., Allen, A., & McCray, R. 2000, *ApJ*, 542, 914
- Wilms, J., Allen, A., & McCray, R. 2000, *ApJ*, 542, 914
- Xu, Y., Baloković, M., Walton, D. J., et al. 2017, *ApJ*, 837, 21
- Yang, Q.-X., Xie, F.-G., Yuan, F., et al. 2015, *MNRAS*, 447, 1692
- Zdziarski, A. A., Johnson, W. N., & Magdziarz, P. 1996, *MNRAS*, 283, 193
- Zdziarski, A. A., Lightman, A. P., & Maciolek-Niedźwiecki, A. 1993a, *ApJL*, 414
- Zdziarski, A. A., Poutanen, J., & Johnson, W. N. 2000, *ApJ*, 542, 703
- Zdziarski, A. A., Zycki, P. T., & Krolik, J. H. 1993b, *ApJL*, 414, L81
- Zdziarski, A. A., Jourdain, E., Lubiński, P., et al. 2021, *ApJL*, 914, L5